Materials Advances

ROYAL SOCIETY OF CHEMISTRY

PAPER

View Article Online
View Journal | View Issue

Check for updates

Cite this: *Mater. Adv.*, 2026, 7, 813

Graphene-PVDF composite membrane for piezoelectric nanogenerators and lithium-ion batteries

Ashok Kushwaha, *[ab] Anu Teresa Peter,[a] Faiz Ullah Shah *[b] and Dipti Gupta *[a]

Received 26th August 2025,
Accepted 21st November 2025

DOI: 10.1039/d5ma00960j

rsc.li/materials-advances

Herein, we introduce a composite membrane comprising polyvinylidene fluoride/graphene nanosheets (PVDF/graphene) for applications in piezoelectric nanogenerators (PENGs) and lithium-ion batteries (LIBs), where the graphene nanosheets play a vital role in enhancing the piezoelectric properties, surface energy, and porosity. A comparative analysis of the pure PVDF and the PVDF/graphene is conducted to evaluate their piezoelectric performance and suitability as separators in LIBs. The PVDF/graphene composite membrane produced a significantly improved piezoelectric output of ~10.8 V under a force of 75 N, while the pure PVDF membrane exhibited only ~3.7 V under the same conditions. Additionally, the Li//PVDF/graphene//graphite half-cell retained ~81.3% of its specific capacity and maintained a coulombic efficiency of over 99.2% after 100 cycles at a 0.2 C rate. In contrast, the Li//pure PVDF//graphite half-cell retained only ~48.6% specific capacity. Furthermore, in a full-cell configuration, the graphite//PVDF/graphene//LCO cell demonstrated excellent stability, retaining ~88% of its specific capacity after 50 cycles, whereas the cell with pure PVDF membrane retained only 38%. Therefore, the PVDF/graphene nanosheet composite membrane has the potential to be used as a piezoelectric membrane in PENGs and as a separator in LIBs.

Open Access Article. Published on 03 December 2025. Downloaded on 2/12/2026 1:54:57 PM.
This article is licensed under a Creative Commons Attribution-NonCommercial 3.0 Unported Licence.

Introduction

Wearable electronic devices are widely explored for applications such as smartwatches, healthcare devices, and other portable devices due to their comfort and lightweight design.[1–3] However, developing flexible, lightweight power sources for these devices remains a research challenge. Piezoelectric and triboelectric generators, as well as self-charging power cells, are the best options to meet the requirements for such devices.[4]

Recent progress has facilitated the development of promising PENGs for use as self-powered devices. These systems are typically lightweight, compact, flexible, and compatible with diverse substrates, which enhances their suitability for a wide range of applications, including gas sensing, biomedical monitoring, environmental detection, ultraviolet (UV) sensing, and integration into the Internet of Things (IoT).[5] PENGs function as energy harvesters by converting ambient mechanical energy, including human motion, acoustic vibrations, and other energy, and transforming it into electrical energy. Their operation relies on the piezoelectric effect, in which certain materials generate an electrical charge when subjected to mechanical stress.[6–10]

The pure PVDF and composite PVDF membranes have been extensively examined for their suitability in energy harvesting and as a piezoelectric separator in alkali metal-ion batteries, owing to their excellent piezoelectric properties, as well as their thermal and electrochemical performance.[1,11–14] PVDF is a promising polymer material for energy harvesting due to its excellent ferroelectric properties, high flexibility, and ease of fabrication in different thicknesses. PVDF exists in multiple crystal phases (α, β, γ, δ, and ε), with the β phase being the essential phase for improving the piezoelectric properties due to its all-trans conformation. The β phase can be promoted through electrical poling, mechanical stress at elevated temperatures, and the addition of filler materials.[15–17] However, pure PVDF exhibits relatively poor piezoelectric, mechanical, and thermal properties, resulting in limited energy harvesting potential and low output voltage. To overcome these challenges, composite PVDF membranes must be developed to improve piezoelectric performance and thermal stability.

Various nanomaterials, including carbon nanotubes, graphene, TiO_2, ZnO, and $BaTiO_3$, have been incorporated into PVDF to

[a] *Plastic Electronics and Energy Laboratory, Department of Metallurgical Engineering and Materials Science, Indian Institute of Technology (IIT) Bombay, Mumbai-400076, India. E-mail: ashok.kushwaha@associated.ltu.se, diptig@iitb.ac.in*

[b] *Chemistry of Interfaces, Luleå University of Technology, SE-971 87 Luleå, Sweden. E-mail: faiz.ullah@ltu.se*

© 2026 The Author(s). Published by the Royal Society of Chemistry

Open Access Article. Published on 03 December 2025. Downloaded on 2/12/2026 1:54:57 PM. This article is licensed under a Creative Commons Attribution-NonCommercial 3.0 Unported Licence.

generate high-performance composite membranes.[18–25] Among these, the PVDF/graphene nanosheets composite porous membranes deliver superior piezoelectric properties, enhanced mechanical ability, and thermal stability, making them highly suitable energy harvester devices and separators in LIBs.[22] In addition to LIBs, commercial separators, typically polypropylene (PP) and polyethylene (PE) membranes, are most common due to their high chemical stability, low cost, and easy preparation.[26] However, these separators often perform poorly in high-temperature applications, exhibiting low thermal stability, poor wettability, and low electrolyte uptake.[11,27–30] Therefore, pristine polymer films alone are inadequate in addressing these issues. A composite polymer membrane offers a promising solution by providing the necessary thermal and mechanical properties for advanced LIB applications.[31]

The composite membrane based on PVDF and graphene demonstrates significant potential for enhancing thermal stability, mechanical stability, and piezoelectric performance. Adding graphene to a PVDF membrane increases the β phase content, improves the wettability, and enhances the electrolyte uptake due to the modified surface energy. The pure PVDF separator, being a hydrophobic surface,[32] exhibited limited wettability of electrolytes, whereas the PVDF/graphene membrane is expected to improve both piezoelectric voltage output and performance as a separator in LIBs.[33,34] In this study, pure PVDF and PVDF/graphene composite membranes were fabricated *via* the solution casting method and subsequently evaluated for their performance in PENGs and LIBs. The composite membrane was prepared by incorporating 0.05 wt% graphene nanosheets, which enhanced both its piezoelectric properties and its performance as a separator in LIBs. The addition of graphene nanosheets is expected to improve the porosity, surface energy, and strength of the PVDF/graphene composite membrane and, thus, improve the overall performance of the battery cell.

Experimental

Materials and methods

The battery-grade materials, including the electrolyte 1 M $LiPF_6$ EC: DEC, graphite, lithium cobalt oxide (LCO), zinc oxide (ZnO), ethanol, and polyvinylidene difluoride (PVDF), were purchased from Sigma Aldrich. The super-p conducting carbon black and *N*-methyl-2-pyrrolidone (NMP) were obtained from Thermo Fisher.

Preparation of the porous PVDF and PVDF/graphene membranes

The porous PVDF membranes were prepared using the drop-casting technique. Initially, PVDF powder was dissolved at 10 wt% in NMP solvent and stirred at 70 °C on a hot plate at 500 rpm for 3 hours to obtain a uniform solution. A PVDF/ZnO solution was prepared by dissolving ZnO powder at an equal mass ratio to the above solution to enhance homogeneity, followed by sonication for 1 hour. The obtained homogeneous solution was drop-cast onto a clean glass substrate at room temperature and dried at 40 °C overnight to form uniform films. The dried films were carefully peeled off from the glass substrate using deionized (DI) water and subsequently dried at 60 °C for 30 minutes. To achieve porosity, the dried films were soaked overnight in a 37% hydrochloric acid solution to remove the ZnO. The films were then rinsed multiple times with DI water until they reached a neutral pH, resulting in uniform porous PVDF films.

For the PVDF/graphene film, 0.05 wt% graphene nanosheets were incorporated into the PVDF/ZnO solution, and further, the same procedure as described above for the preparation of the PVDF membrane. The graphene nanosheets with a thickness of 3–10 nm were synthesized using a solvent exfoliation technique in greener solvents as described in our previous publications.[35,36]

The electrical poling process

The prepared porous PVDF film was placed between ITO-coated PET electrodes and encapsulated with thermal tape to ensure optimal electrode contact. For device preparation, copper wires were attached to both electrodes using silver paste, providing a reliable connection for applying the voltage. The devices were polarized by applying a DC field of 20 kV mm^{-1} at 80 °C for 30 minutes, resulting in an enhanced alignment of dipoles from a random to an organized orientation.

Wettability and ionic conductivity

Porosity is a critical parameter of membranes, directly influencing ion mobility and piezoelectric potential. The porosity of pure PVDF and PVDF/graphene membranes was estimated using the *n*-butanol uptake method, as described in the following equation.[37]

$$\text{Porosity } (\%) = \frac{(w_1 - w_0)}{\rho_b V_0} \quad (1)$$

where w_1 is the mass of the separator after complete uptake of *n*-butanol, w_0 is the mass of the dry separator, and ρ_b is the density of *n*-butanol.

The wettability of the separators was assessed through the electrolyte uptake (E_U) method. The E_U was calculated using the following equation.[38]

$$E_U = \left(\frac{M_S - M_d}{M_d}\right) \times 100\% \quad (2)$$

where the saturated membrane (M_S) is weighted after immersing in *n*-butanol for 12 hours, and the dry membrane (M_d) is weighted before immersing in *n*-butanol, respectively.

The ionic conductivity was evaluated through impedance spectroscopy within a frequency range from 1 Hz to 1 MHz, with an AC voltage amplitude of 10 mVrms. For temperature-dependent measurements, both heating and cooling cycles were performed over a temperature range of −20 to 60 ± 0.1 °C. The following equation was applied to measure

© 2026 The Author(s). Published by the Royal Society of Chemistry

Open Access Article. Published on 03 December 2025. Downloaded on 2/12/2026 1:54:57 PM. This article is licensed under a Creative Commons Attribution-NonCommercial 3.0 Unported Licence.

the ionic conductivity of pure PVDF and PVDF/graphene membranes.[38]

$$\sigma = \frac{d}{R_b A_s} \quad (3)$$

where d and R_b are the thickness and the bulk resistance of the separator, respectively, and A_s is the area of the electrodes.

The transfer number (t^+) was investigated using the electrochemical impedance spectroscopy (EIS) and chronoamperometry testing of Li//Li symmetric cells, according to the following equation.[39]

$$t_{Li^+} = \frac{I_{ss}(\Delta V - I_0 R_0)}{I_0(\Delta V - I_{ss} R_s)} \quad (4)$$

where I_0 and I_{ss} are the initial and steady-state currents, respectively. R_0 and R_s are the interfacial resistance before and after the polarization test. ΔV is the perturbation potential (10 mV).

Material characterization

The thickness and dimensions of the exfoliated graphene nanosheets were evaluated using atomic force microscopy (AFM, Agilent 5500), while their structural distribution was analyzed using Raman spectroscopy (Alpha 300). The surface morphology of the fabricated pure PVDF and PVDF/graphene membranes was examined using field emission scanning electron microscopy (FESEM, Ultra 55). Furthermore, the morphology of the graphite electrode before and after cycling was evaluated using FESEM. Prior to SEM analysis, the cycled cell was disassembled, and the electrode was rinsed three times with dimethyl carbonate (DMC) to remove residual salts and electrolytes, followed by drying in a glove box. Additionally, the phase variation of these membranes, both before and after poling, was investigated using X-ray diffraction (XRD, PANalytical) and Fourier transform infrared spectroscopy (FTIR, Vertex 70 from Bruker). The piezoelectric performance of the developed membrane was assessed using a Force Gauge (Mark-10, ESM303).

Electrode preparation and electrochemical performance

The electrochemical performance was assessed using CR2032 coin cell components, incorporating either the pure PVDF or the PVDF/graphene membrane. For full-cell configurations, LCO was used as the positive electrode, graphite as the negative electrode, and 1.0 M $LiPF_6$ in an EC: DEC as the electrolyte. In the half-cell configurations, graphite was employed as the working electrode, while Li–metal was the counter and reference electrode. All the cells were assembled in an argon-filled glovebox with oxygen and moisture levels maintained below 0.1 ppm. The electrodes were fabricated using the doctor blade coating method. For the fabrication of the positive electrode, a homogenous slurry was prepared by mixing 80% LCO as the active material, 10% carbon black as the conductive agent, and 10% PVDF as the binder. The resultant slurry was coated onto an aluminum foil and dried in a vacuum oven at 90 °C for 12 hours. Further, it was punched into 14 mm disks and stored in the glovebox for testing. The negative electrode was fabricated following a similar process to that employed for the positive electrode, with graphite serving as active material. It was then punched into a 16 mm diameter disk for testing in a coin cell. The mass loadings on the positive and negative electrodes were 5.6 mg cm^{-2} and 2.6 mg cm^{-2}, respectively, with an N/P ratio of approximately 1.15 for the full cell. A volume of 70 μL of electrolytes was used during assembly of both half and full coin cells. The electrochemical testing of the assembled full cell was conducted within a voltage range of 2.6–4.2 V at a current density of 0.1C.

Symmetrical Li//Li cells were fabricated using the same electrolyte, 14 mm lithium metal, and either pure PVDF or PVDF/graphene membranes. Further, they were tested at a current density of 1 mA cm^{-2} with a capacity of 1 mAh cm^{-2}. All the electrochemical characterizations were conducted using Autolab 204 (Metrohm) and VMP3 (Biologic) electrochemical stations.

Results and discussion

We start with a description of the fabrication of pure PVDF and composite PVDF/graphene membranes using solution casting techniques, and then their structural characterization. Next, we evaluate the porosity, ionic conductivity, phase variation with the inclusion of graphene nanosheets, as well as the effect of electric poling on the membranes. Further, the piezoelectric properties of pure and composite PVDF/graphene membranes will be analyzed and compared. Finally, we assess and discuss the electrochemical performance of these membranes using symmetric Li//Li cells, half Li//graphite cells, and full graphite//LCO cells.

Preparation and characterization of the membranes

The porous PVDF/graphene membrane was prepared *via* a solution-casting process. A mixed solution of PVDF, ZnO, and 0.05 wt% of graphene nanosheets was prepared by mechanical stirring and cast over a glass substrate, followed by acid etching to eliminate the ZnO particles, as shown schematically in Fig. 1. The ZnO nanoparticles were used as seed crystals to control the crystallinity of the polymer to develop the porous membrane and assist in generating the β-phase formation. However, pure porous PVDF is inefficient in fulfilling energy harvesting requirements and as a separator in LIBs. Hence, an additive needs to be added to the PVDF membrane to improve the required properties, and herein, we introduced low percentages of graphene nanosheets as an additive to the porous PVDF membrane to enhance its piezoelectric and separator properties. The fabrication of the pure porous PVDF membrane followed the same procedure as that used for the PVDF/graphene membrane shown in Fig. 1. The thickness of pure PVDF and PVDF/graphene film was measured to be ~30 and ~32 μm, respectively, and is suitable for the intended applications. The optical images of the prepared pure PVDF and composite PVDF/graphene membranes are shown in Fig. S1. The optical image of the porous PVDF/graphene membrane

Open Access Article. Published on 03 December 2025. Downloaded on 2/12/2026 1:54:57 PM.
This article is licensed under a Creative Commons Attribution-NonCommercial 3.0 Unported Licence.

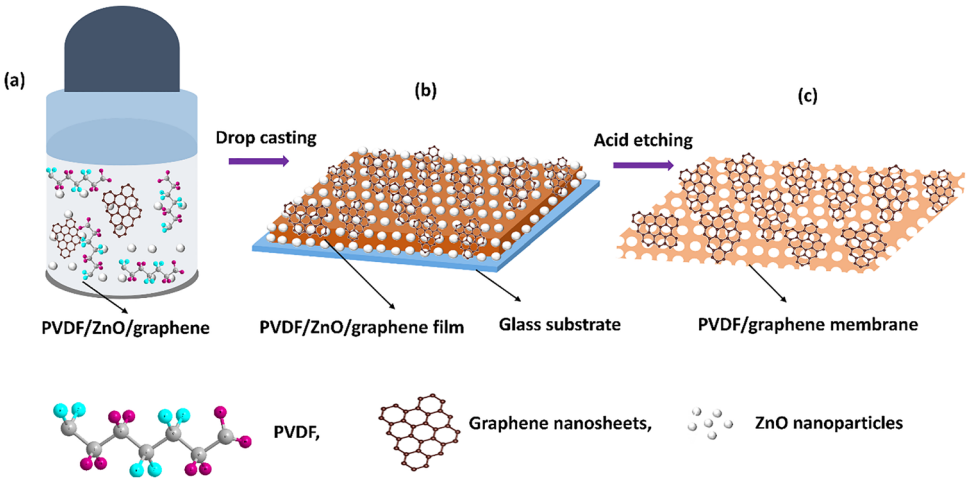

Fig. 1 The schematic illustration represents the preparation process of the PVDF/graphene membrane. (a) The mixed solution of PVDF, ZnO, and graphene; (b) the mixed PVDF/ZnO/graphene solution cast over a glass substrate as a film; and (c) the porous PVDF/graphene membrane after acid etching.

shows a uniform composite film, which is appropriate for enhancing the piezoelectric output performance, as well as a separator in LIBs.

The physical characterization of the prepared graphene nanosheets is presented in Fig. S2. XRD analysis shows that the graphene nanosheets exhibit broader and lower-intensity peaks compared to the sharp, high-intensity peak of the graphite at a 2θ angle of $\sim 26.3^{\circ}$ (corresponding to the 002 plane), confirming the successful exfoliation of the graphene from graphite (Fig. S2a).[40,41] Raman spectroscopy further confirms the structural analysis, revealing characteristic D, G, and 2D peaks at 1340, 1586, and 2380 cm^{-1}, respectively (Fig. S2b). The calculated I_D/I_G ratio of ~ 0.35 suggests that the graphene nanosheets are well-ordered and possess minimal structural defects. The AFM topography images of the exfoliated graphene nanosheets show lateral sizes ranging from 3 to 10 nm (Fig. S2c and d). These findings indicate that the graphene nanosheets produced using this greener approach are highly ordered and exhibit minimal defects, making them well-suited for enhancing both the piezoelectric properties and the porosity of membranes.[42,43]

Fig. 2a and b displays the SEM images of the porous pure PVDF and PVDF/graphene films, illustrating their morphology. The top-view morphological image of pure PVDF film in Fig. 2a reveals the diverse structure and pore size distribution, indicating the complete removal of ZnO nanoparticles post-acid etching without harming the film structure. However, non-uniform pore size distribution in pure PVDF may impede the piezoelectric output performance and ion movements in LIBs. Further, a higher magnification image of pure PVDF membrane, illustrating the non-uniform and low porosity structure. The SEM image in Fig. 2b, which depicts the top-view morphology of the PVDF/graphene membrane, exhibits a comparable structure to the pure PVDF membrane but exhibits secondary porosity. In the higher magnification SEM image, it is seen that the graphene nanosheets are uniformly incorporated with PVDF monomer, which effectively promotes a better channel formation for the movement of lithium-ions. The lower and higher magnification SEM images of PVDF/graphene composite film show higher porosity than the pure PVDF film, contributing to their change in surface energy. The non-uniform distribution of pores in the pure PVDF, when compared to the PVDF/graphene, can be seen distinctly in the lower magnification SEM images, as shown in Fig. S3(a) and (b). The highly porous nature of PVDF/graphene film facilitates improved contact with the electrode interface and uptake of electrolytes in LIB systems. It potentially enhances the piezoelectric voltage output performance. Consequently, the PVDF/graphene films developed in this work can improve the performance of LIBs and energy harvesting devices.

The ionic conductivity of a battery cell is influenced not only by the electrolyte but also by the electrolyte uptake capability of the separator.[29,44] Therefore, the wettability of the separator plays a critical role in facilitating Li-ion migration, as it is governed by the separator's surface energy and porosity. Porosity measurements were carried out using the *n*-butanol uptake method, which revealed that the PVDF separator with 0.05 wt% graphene exhibited a high porosity of $\sim 38\%$, compared to 26% of the pure PVDF. However, increasing the graphene content to 1 wt% reduced porosity to around 22%.

Notably, the PVDF/graphene separator containing 0.05 wt% graphene exhibits a significantly lower bulk resistance ($\sim 4.7\ \Omega$) compared to pure PVDF ($\sim 56\ \Omega$), as shown in Fig. S4(a) and (b). Consequently, its ionic conductivity calculated using eqn (3) (~ 0.34 mS cm^{-1}) is substantially higher than the value observed for the pure PVDF (~ 0.18 mS cm^{-1}).

The ionic conductivity was evaluated across different graphene loadings, with the membrane containing 0.05 wt% graphene exhibiting the highest ionic conductivity of ~ 0.34 mS cm^{-1}. This enhancement is attributed to the improved porosity of the membrane at this composition, which facilitates efficient ionic transport. However, further increases in graphene content beyond 0.1 wt% resulted in elevated bulk resistance and decreased ionic

© 2026 The Author(s). Published by the Royal Society of Chemistry

Open Access Article. Published on 03 December 2025. Downloaded on 2/12/2026 1:54:57 PM.
This article is licensed under a Creative Commons Attribution-NonCommercial 3.0 Unported Licence.

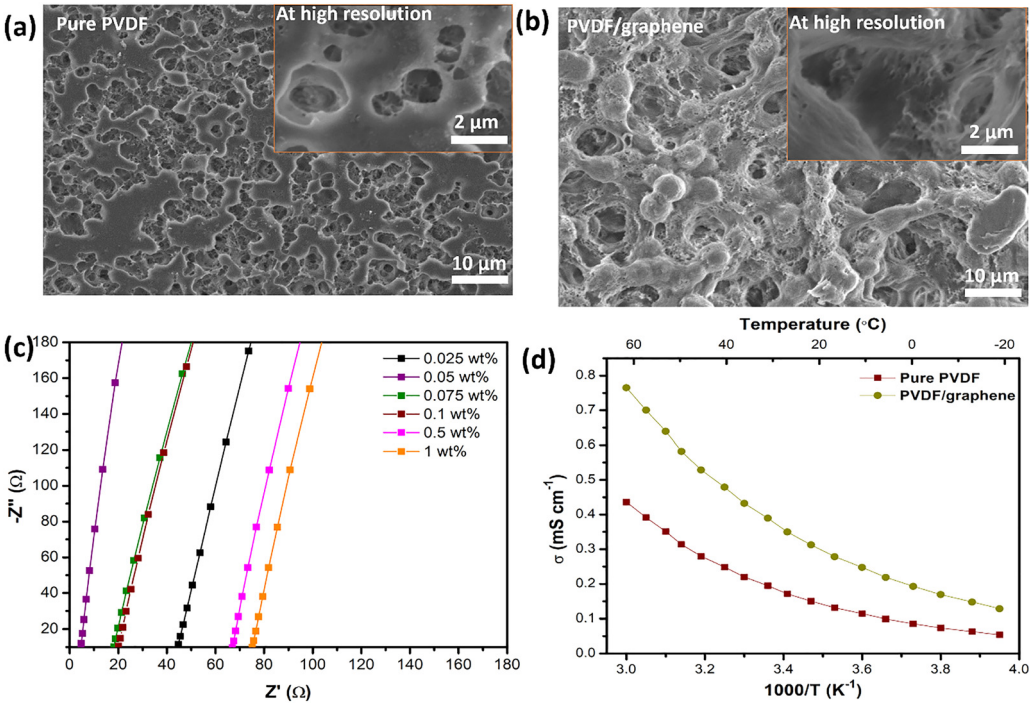

Fig. 2 (a and b) SEM images of pure PVDF and PVDF/graphene membranes at lower and higher magnifications, respectively. (c) The EIS spectra of PVDF/graphene membranes with different graphene contents, (d) and ionic conductivity of the pure PVDF and PVDF/graphene membranes as a function of temperature.

conductivity (Fig. 2c and Fig. S5). This decline in performance is likely due to reduced membrane porosity at higher filler concentrations, which hinders Li^+ ion mobility through the separator matrix.[45] Fig. S6(a) and (b) shows that increasing the thickness of the PVDF/graphene membrane leads to higher bulk resistance, resulting in reduced ionic conductivity. This suggests that the lithium-ion transport path length increases with membrane thickness, thereby impeding ion mobility through the separator.[46]

Furthermore, ionic conductivity of the pure PVDF and PVDF/graphene membranes (0.05 wt%) was evaluated at various temperatures, along with their activation energies (E_a) determined using the Arrhenius fitting method (Fig. 2d). The PVDF/graphene composite membrane exhibited higher ionic conductivity than the pure PVDF membrane across all temperatures. Additionally, the PVDF/graphene membrane showed a significantly lower activation energy of 12.05 kJ mol^{-1} compared to 63.29 kJ mol^{-1} for the pure PVDF (Table S1). These findings demonstrate that incorporation of 0.05 wt% graphene nanosheets greatly enhances the wettability (as evaluated by eqn (2)) of the PVDF membranes, resulting in improved ionic conductivity and piezoelectric performance. These results highlight the potential of the PVDF/graphene composite as a high-performance membrane for LIBs.

The XRD and FTIR tests were conducted to confirm the effects of poling and fillers of nanocomposite graphene on the PVDF phase. The XRD patterns of the pure PVDF and the composite PVDF/graphene membranes before and after poling are shown in Fig. 3a. The α-phase appears at 18.1° in XRD patterns of all the PVDF membrane films, corresponding to the reflection of 020 and 110 planes. However, the XRD pattern of PVDF powder shows two α-phase peaks at 18.1° and 19.4°, as seen in Fig. S7. One among the α-phase peaks disappeared in the cases of pure PVDF and nanocomposite PVDF/graphene membrane films, and a new peak of β-phase appeared at 20.4°, which corresponds to the reflection of the 110 and 200 planes, respectively. It can be assumed that the PVDF monomers have interacted with the NMP solvent molecules, and their dipoles have become self-polarized.[47] Therefore, the pure PVDF membrane does not show much change in angle or intensity before and after poling. In contrast, after poling, the graphene nanocomposite PVDF membrane shows two β-phase peaks: one high-intensity peak at 20.4° and a small peak at 38.2°. The appearance of higher degree peaks may be due to the reflection of 300 and 020 planes, respectively. Thus, the pre-poled and post-poled PVDF membrane shows low-intensity peaks, indicating a low percentage of β-phase compared to the post-poled PVDF/graphene membrane. Hence, the graphene nanosheets can help to enhance the percentage of β-phase, which will be useful for creating high piezoelectric potentials.

The FTIR spectra of pure PVDF and PVDF/graphene membranes before and after poling, highlighting their phase transformations, are shown in Fig. 3b. FTIR spectra are applied to analyze the structure of PVDF chains with and without the incorporation of graphene nanosheets. The presence of the β-phase was confirmed by the absorption bands at 510 cm^{-1} and 1276 cm^{-1}. The absorption band at 840 cm^{-1} is attributed exclusively to poled pure PVDF, pre-poled PVDF/graphene, and

Open Access Article. Published on 03 December 2025. Downloaded on 2/12/2026 1:54:57 PM.
This article is licensed under a Creative Commons Attribution-NonCommercial 3.0 Unported Licence.

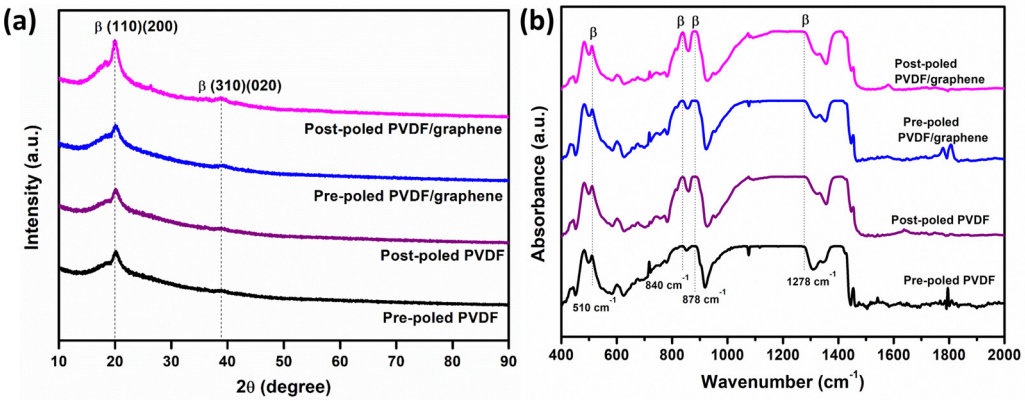

Fig. 3 (a) XRD pattern of the pure PVDF and PVDF/graphene membranes before and after poling. (b) The comparison of FTIR spectra among pre-poled pure PVDF, post-poled pure PVDF, pre-poled PVDF/graphene, and poled PVDF/graphene membranes.

post-poled PVDF/graphene samples and is absent in the pure PVDF films. The β-phase transformation mechanism involves CF_2 bending (bands at 510 cm^{-1}) and CH_2 rocking (bands at 840 cm^{-1}). The composite PVDF/graphene film exhibits a reduced amount of alpha phase due to the specific and strong electrostatic interactions between the graphene nanosheets and the hydrogen groups in the PVDF chains. The β-phase fraction (F_β) of all samples was quantitatively determined using the Lambert–Beer law.[48] The absorbance peaks at 764 cm^{-1} (α-phase) and 840 cm^{-1} (β-phase) in the FTIR spectra were used to calculate the F_β value.[49]

$$F_\beta = \frac{A_\beta}{\left(\frac{k_\beta}{k_\alpha}\right)A_\alpha + A_\beta} \times 100\%$$

where A_α and A_β the absorption values at 764 cm^{-1} and 840 cm^{-1}, respectively, and k_β and k_α, are their corresponding absorption coefficient. In this study, $k_\alpha = 6.1 \times 10^4$ cm^2 mol^{-1} and, $k_\beta = 7.7 \times 10^4$ cm^2 mol^{-1} were used.[48,49] The calculated F_β values for pure PVDF, poled PVDF, PVDF/graphene, and poled PVDF/graphene membranes were 52%, 62%, 58%, and 74%, respectively. These results confirm that the incorporation of graphene nanosheets enhances the β-phase formation in PVDF, while the poling process further promotes dipole alignment, leading to higher β-phase content and improved piezoelectric performance.

The piezoelectric output performance

To further investigate the piezoelectric output performance of the pure PVDF and the PVDF/graphene composite films, devices were fabricated using these membranes, and their output was measured under a range of applied forces. A device of the size 1.5 cm^2 was fabricated and was maintained at constant force throughout the test. The optical image of the fabricated device is provided in Fig. S8. To evaluate the piezoelectric output performance of the pure PVDF and PVDF/graphene membranes before and after poling, compressive mechanical forces were applied using the Mark-10 force gauge, and the output was simultaneously recorded with the oscilloscope. Generally, applying force to the PVDF film creates mechanical stress along the polarization axis, which increases the membrane strain and induces a temporary flow of free electrons in the piezoelectric field, generating the forward signal. When the force is removed, an opposite electric potential is created as free electrons accumulate on both sides of the membrane. This opposite electric field causes electrons to flow in reverse, generating a backward signal.

The peak-to-peak piezoelectric output voltage for the poled pure PVDF membrane was ~2.7 V at a low force of 22 N. When the applied force was increased from 22 to 75 N, the peak-to-peak voltage amplified from 2.7 to 3.7 V (Fig. 4a). However, this output performance showed a minimal increase (3.2–3.7 V) between 50 N, and 75 N forces, indicating a lower percentage of the β-phase content in the poled pure PVDF (Fig. 4b and c). In contrast, the poled porous pure PVDF membrane exhibited complete piezoelectric actions with two reverse polarizations and maintained stable behavior under a constant force (Fig. 4a–c). As illustrated by the error bar graph in Fig. 4d, only minor variations in piezoelectric voltage output were observed for applied forces of 22 N, 50 N, and 75 N. On the contrary, the pre-poled pure PVDF membrane generated less than 2 V even at a higher applied force of 75 N, as depicted in Fig. S9. These results highlight that poling enhances the β-phase content in the PVDF membrane, improving the piezoelectric voltage output performance. Nevertheless, due to the relatively low output performance of pure PVDF, it is not very reliable for use in self-charging energy storage and power devices. Therefore, to improve the piezoelectric output performance, additives are required.

In stark contrast, the incorporation of graphene nanosheets into PVDF membranes was investigated as a method to enhance the piezoelectric output performance. The piezoelectric performance of the porous PVDF/graphene membrane, both pre- and post-poled, was evaluated under the same applied compressive forces used earlier for the pure PVDF membrane. Peak-to-peak output voltage performance of PVDF/graphene membranes yielded values of 1.8 V at 22 N, 7.2 V at 50 N, and 10.8 V at 75 N (Fig. 5a–c). After poling, the reversible output voltage at a force of 75 N of the PVDF/graphene membrane was ~2.8 times higher than that of the post-poled

© 2026 The Author(s). Published by the Royal Society of Chemistry

Open Access Article. Published on 03 December 2025. Downloaded on 2/12/2026 1:54:57 PM.
This article is licensed under a Creative Commons Attribution-NonCommercial 3.0 Unported Licence.

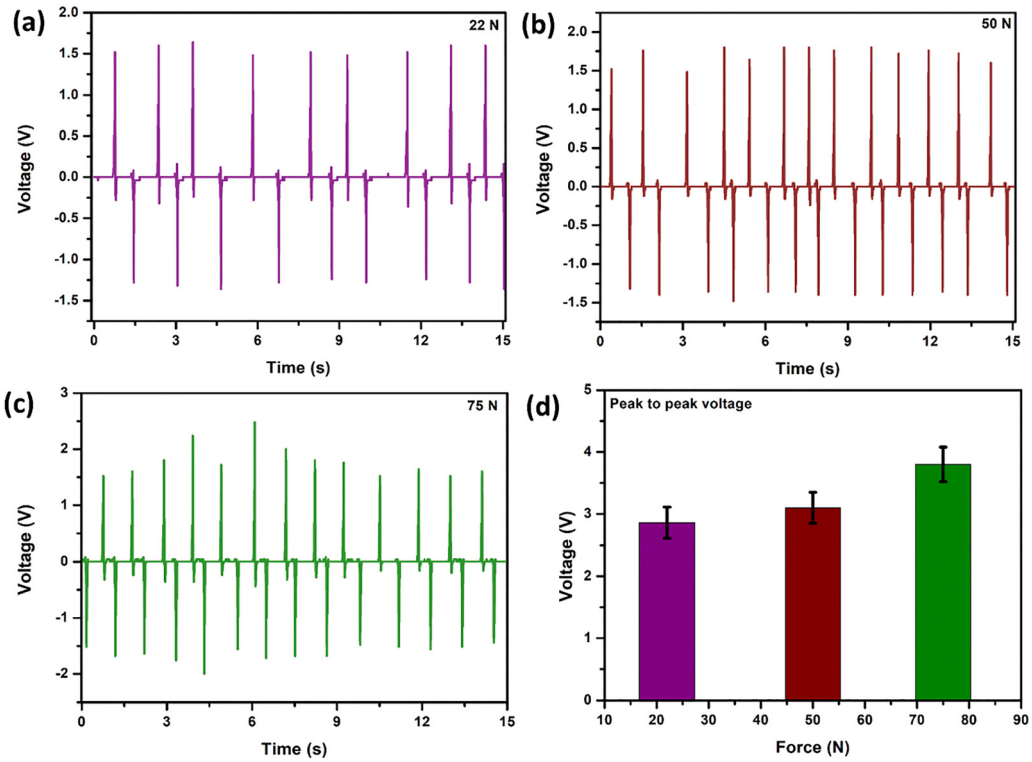

Fig. 4 The piezoelectric voltage output performance of the post-poled PVDF membrane under different applied forces. (a) at 22 N force, (b) at 50 N force, (c) at 75 N force. (d) Represents the variation of piezoelectric output voltage with the applied forces.

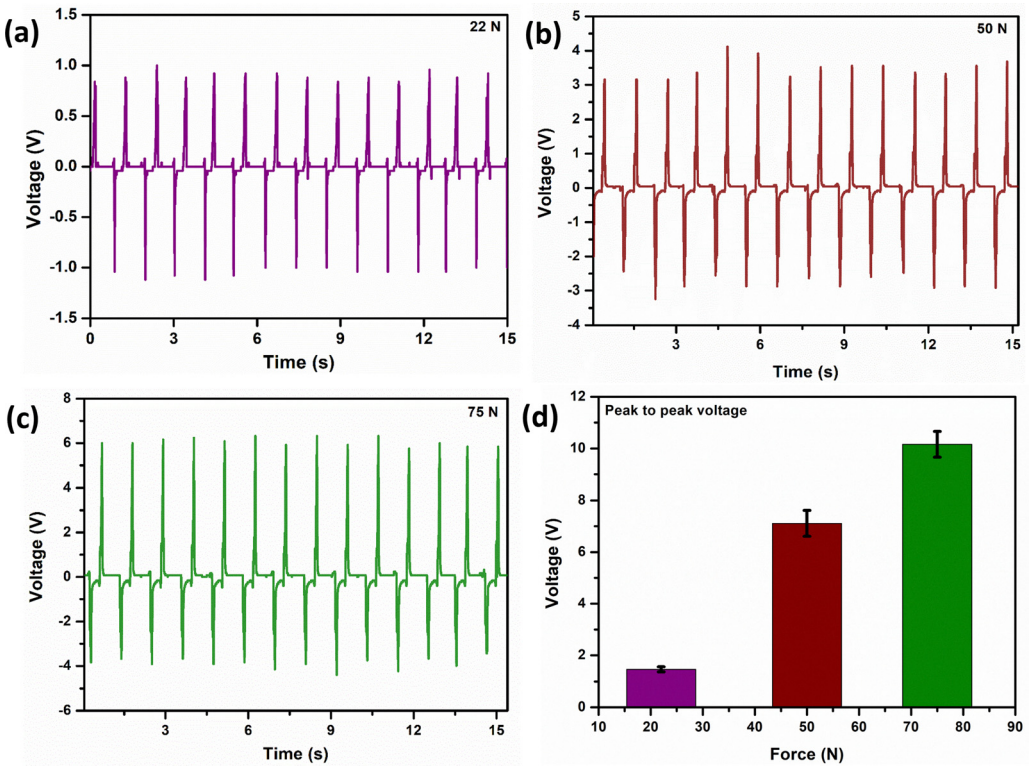

Fig. 5 The piezoelectric output voltage performance of the post-poled PVDF/graphene composite membrane under different applied forces. (a) at 22 N force, (b) at 50 N force, (c) at 75 N force. (d) The variation of piezoelectric output voltage with the applied forces.

Open Access Article. Published on 03 December 2025. Downloaded on 2/12/2026 1:54:57 PM. This article is licensed under a Creative Commons Attribution-NonCommercial 3.0 Unported Licence.

pure PVDF membrane. This substantial enhancement in peak-to-peak voltage for the post-poled PVDF/graphene membrane is attributed to a high β-phase content following the poling process. In contrast, a pre-poled PVDF/graphene membrane generated only ~3.9 V, nearly equal to the poled PVDF membrane (Fig. S10). The presence of graphene in the PVDF matrix increases the β-phase content due to the electrostatic interactions between sp^2-hybridized carbon atoms in graphene and the hydrogen atoms in the PVDF chain.[22,50,51] The high electronegativity of carbon, relative to hydrogen atoms, induces interaction between hydrogen atoms from the $-CF_2/-CH_2$ chain and the graphene surface.

Additionally, the conductivity of graphene significantly boosts the local electric field and inductive charge, which tends to create a strong coulombic force. This force aligns the randomly oriented dipoles within PVDF to form a parallel β-phase alignment along the graphene surface, a phenomenon described as alpha-to-beta phase transformation.[13,52] The output peak-to-peak voltage of the composite membrane increased progressively with applied compressive force (Fig. 5d). Thus, the addition of graphene nanosheets and the increase in porosity of the PVDF membrane can improve its piezoelectric performance. In a porous composite matrix, the intermolecular interactions between graphene and PVDF reduce phase separation while promoting efficient stress transfer and amplification. These interactions lead to an increased β-phase content, as verified by XRD and FTIR analyses. As a result, the PVDF/graphene composite membrane demonstrates a notable enhancement in piezoelectric performance.[53]

Composite PVDF films often exhibit low stiffness, which can hinder uniform stress distribution within the PVDF matrix and consequently reduce piezoelectric output performance under smaller applied forces. Additionally, the incorporation of conductive fillers into PVDF may create conductive pathways, leading to leakage currents and a reduction in the internal electric field generation. In contrast, pure PVDF possesses a well-defined molecular structure after poling, exhibiting a dominant active crystalline phase and a high intrinsic piezoelectric coefficient (d_{33}) at lower applied forces.[54,55] Thus, the integration of graphene within PVDF membranes presents a promising approach for application in self-charging batteries, supercapacitors, and other energy-harvesting devices.

Electrochemical performance

To assess the effectiveness of pure PVDF and PVDF/graphene membranes in controlling lithium dendrite formation, lithium symmetric cells were tested under a current of 1 mA cm^{-2} and a 1 mAh cm^{-2} capacity (Fig. 6a). The PVDF/graphene membrane exhibited an average overpotential of 20 mV after 250 hours, while the pure PVDF membrane suffered short-circuiting after just 20 cycles. Notably, the PVDF/graphene membrane maintained a stable overpotential even after 5 cycles, demonstrating

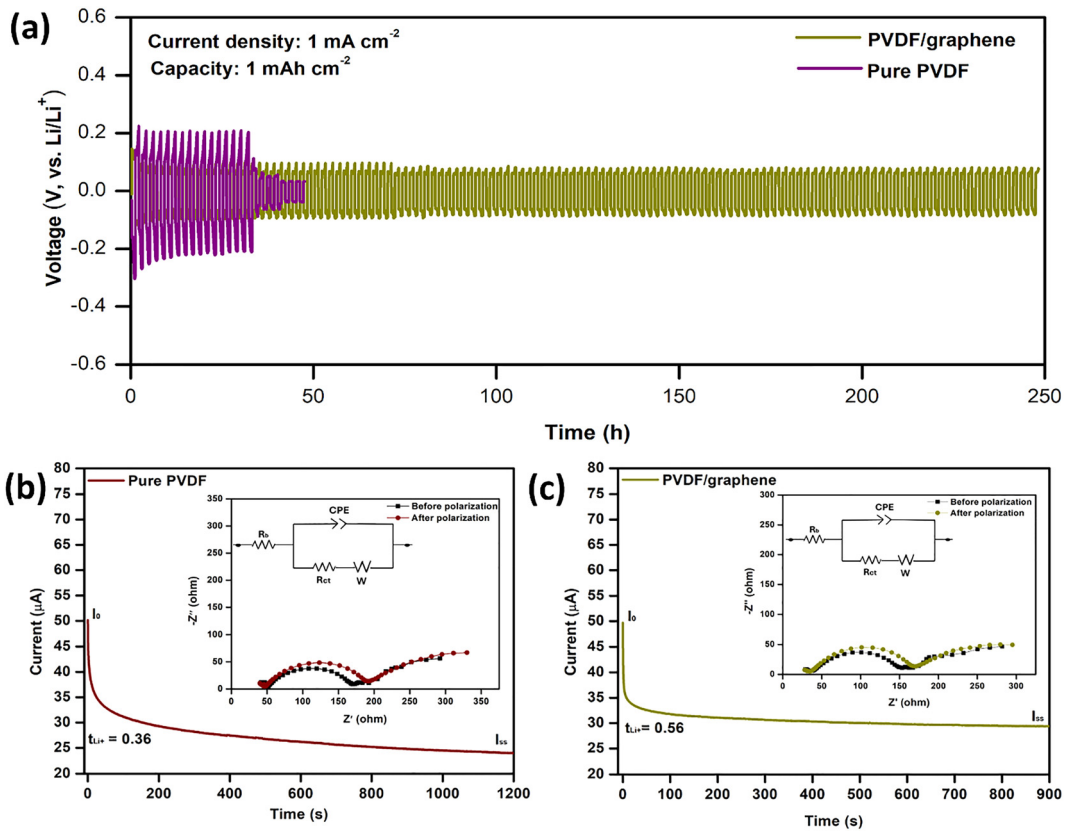

Fig. 6 (a) Galvanostatic plating/stripping cycling of a symmetric Li//Li cell, (b) and (c) chronoamperometry profiles of the Li//Li cells under applied perturbation voltage of 10 mV using the pure PVDF and PVDF/graphene separators.

 © 2026 The Author(s). Published by the Royal Society of Chemistry

Open Access Article. Published on 03 December 2025. Downloaded on 2/12/2026 1:54:57 PM.
This article is licensed under a Creative Commons Attribution-NonCommercial 3.0 Unported Licence.

its ability to suppress electrolyte consumption and inhibit lithium dendrite growth throughout cycling. In contrast, the failure of the pure PVDF membrane is likely due to rapid electrolyte depletion, side reactions, and increased polarization with continued cycling. These findings suggest that the PVDF/graphene membrane effectively mitigates dendrite formation and facilitates smooth ion transport.

More importantly, graphene nanosheets play an important role in improving the mechanical properties and supporting the local stress of the PVDF membrane, potentially increasing the overall strength of films. The lithium transfer number (t_{Li^+}) test was conducted to evaluate the contribution of Li-ion migration in ionic conductivity using chronoamperometry (Fig. 6b and c). The t_{Li^+} of the PVDF/graphene-based separator was found to be 0.56, which is higher than that of pure PVDF ($\sim$0.36) and that of the commercial separator ($\sim$0.4).[26,56] This indicates that the addition of graphene nanosheets in PVDF could improve the t_{Li^+}.

The cyclic voltammograms (CV) of graphite electrodes with a pure PVDF and PVDF/graphene separators over three cycles at a scan rate of 0.1 mV s^{-1} within a potential range of 0.01–2 V are shown in Fig. 7(a) and (b). In the first cycle CV, the cell with the pure PVDF separator exhibits electrolyte decomposition around 0.8 V during the cathodic scan, leading to the formation of solid electrolyte interface (SEI).[35,57] From the first cycle onwards, Li-ion intercalation into the graphitic carbon electrode occurs

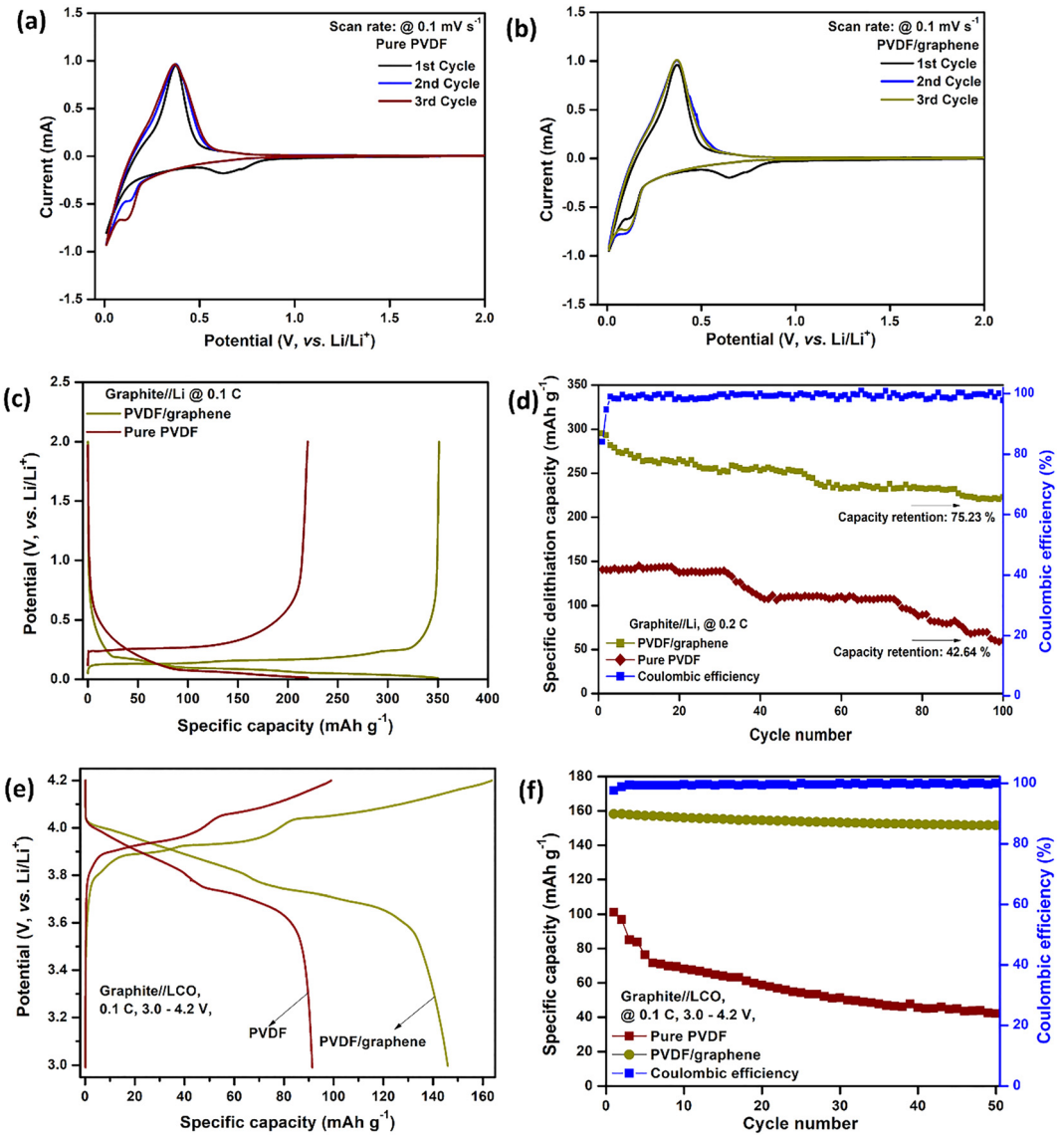

Fig. 7 Electrochemical performance of the Li//graphite cells using pure PVDF and the PVDF/graphene membranes as separators. (a) CV of the cell using the pure PVDF membrane, (b) CV of the cell using the PVDF/graphene membrane, (c) comparative voltage spectra of cell using the pure PVDF and the PVDF/graphene membranes, and (d) cyclic stability performance of the cells using the pure PVDF and the PVDF/graphene membranes along with coulombic efficiency corresponding to the PVDF/graphene membrane. Electrochemical performance of the full cell, (e) and (f) initial voltage spectra, and cyclic stability performance using the pure PVDF and the PVDF/graphene separators.

Open Access Article. Published on 03 December 2025. Downloaded on 2/12/2026 1:54:57 PM.
This article is licensed under a Creative Commons Attribution-NonCommercial 3.0 Unported Licence.

at lower potentials around 0.3–0.01 V *vs.* Li/Li^+, as shown in Fig. 7(a). Notably, the first cathodic scan with the pure PVDF separator at a lower potential of 0.3–0.01 V *vs.* Li/Li^+ exhibits a smoother profile, suggesting thicker and non-uniform SEI formation. In contrast, the PVDF/graphene separator facilitates more uniform SEI formation and stable, reversible cycling from the first cycle (Fig. 7b). Moreover, distinct, reversible cathodic peaks at lower potentials around 0.25 V with the PVDF/graphene separator confirm consistent and reversible lithium-ion intercalation into the graphite electrodes.

Fig. 7(c) represents the charge–discharge cycling performance of graphite electrodes using PVDF and PVDF/graphene separators within a potential range of 0.01–2 V at a 0.1C rate. The PVDF/graphene separator achieved a deintercalation-specific capacity of 335 mAh g^{-1}, compared to 157 mAh g^{-1} with the pure PVDF separator. Therefore, the PVDF/graphene membrane has promising potential as a separator in Li-ion systems due to enhanced specific capacity retention and improved interfacial compatibility with the electrodes. Additionally, the PVDF/graphene separator maintained ~81.3% of its deintercalation-specific capacity after 100 cycles at a 0.2C rate, whereas the pure PVDF retained only 48.6% (Fig. 7d). Furthermore, cells with the PVDF/graphene separator demonstrated an initial coulombic efficiency of over 85%, which increased to ~99% after 100 cycles.

The rate capability of the Li//graphite cell incorporating the PVDF/graphene membrane was evaluated at current rates ranging from 0.1C to 2C, followed by a return to 0.1C, as shown in Fig. S11(a). The specific charge capacities were 356.4, 312.2, 254.8, 197.8, and 57.0 mAh g^{-1} at current rates of 0.1C, 0.2C, 0.5C, 1C, and 2C, respectively, indicating that the PVDF/graphene as a separator maintains functionality even under high current conditions. Upon returning to 0.1C, the specific capacity recovered to ~340 mAh g^{-1}, which is comparable to the initial capacity at 0.1C. The voltage profiles shown in Fig. S11(b) further confirm the good reversibility and capacity retention at 0.1C. This performance clearly demonstrates that the PVDF/graphene composite membrane possesses a uniform and stable porous structure, where the graphene nanosheets are evenly dispersed and interconnected within the pore channels. Such a structural configuration facilitates enhanced Li-ion transport, as supported by SEM observations and ionic conductivity measurements. In addition, both prepared membranes were evaluated in full LIB cells. Before assembling the full cell, graphite and LCO electrodes were tested in a half-cell LIB system to determine the capacity ratio (*e.g.*, obtained N/P = 1.15). The first cycle of charge–discharge electrochemical performance of the LCO//Li half-cell is presented in the SI (Fig. S12). In the initial discharge cycle, the LCO electrode achieved a specific capacity of 128 mAh g^{-1} within a voltage range of 2.6–4.2 V at a 0.2C rate.

The full cell using a PVDF/graphene membrane delivered an initial discharge capacity of ~148 mAh g^{-1}, whereas the cell using a pure PVDF membrane achieved only ~94 mAh g^{-1} (Fig. 7e). This improvement suggests that graphene in the PVDF matrix facilitates Li-ion transport properties, enhances interfacial contact between electrode and separator, inhibiting dendrite formation, and ultimately improves the LIBs performance.

The cyclic stability of the full cell using both pure PVDF and PVDF/graphene separators was evaluated at 0.1C within the same voltage range (Fig. 7f). After 50 cycles, the PVDF/graphene-based separator retained ~88% of its specific capacity, whereas the porous pure PVDF separator retained only about 38%. These findings underscore the significant role of

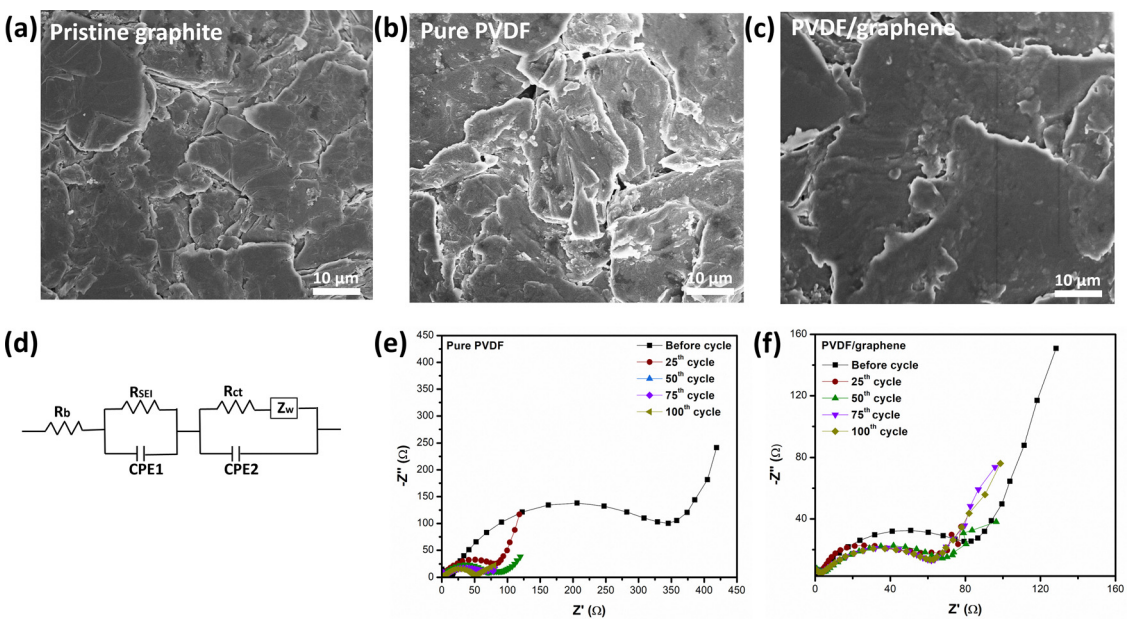

Fig. 8 SEM images of the graphite electrode before and after 100 cycles at a 1C rate: (a) pristine graphite, (b) pure PVDF, and (c) PVDF/graphene. (d) Equivalent circuit model used for EIS fitting, and (e) and (f) EIS spectra of Li//graphite cells after various cycling numbers at a 1C rate using pure PVDF and PVDF/graphene membranes.

© 2026 The Author(s). Published by the Royal Society of Chemistry

Open Access Article. Published on 03 December 2025. Downloaded on 2/12/2026 1:54:57 PM. This article is licensed under a Creative Commons Attribution-NonCommercial 3.0 Unported Licence.

the PVDF/graphene separator in enhancing battery performance, supporting its application in PENGs, and high-temperature LIBs. The reported PVDF membranes with various compositions and their performance in different types of battery cells, along with the results obtained for the PVDF/graphene membrane, are summarized in Table S2.

The SEM analysis was conducted to evaluate the morphological changes of the graphite electrode before and after cycling. The morphology of the pristine graphite electrode shows well-distributed and interconnected graphite particles (Fig. 8a). After cycling with the pure PVDF membrane, slight morphological degradation and particle aging were observed (Fig. 8b). In contrast, the graphite electrode cycled with the PVDF/graphene membrane exhibited a more compact and uniform morphology, with a stable SEI layer (Fig. 8c). This suggests that the PVDF/graphene membrane provides better interfacial contact and promotes the formation of a stable SEI.

Furthermore, the EIS fitting model shown in Fig. 8d was employed to analyze the interfacial resistance, where R_b represents the bulk resistance, R_{sei} and R_{ct} corresponding to the SEI and charge transfer resistance, respectively, while CPE1 and CPE2 denote associated capacitance.[58,59] The Nyquist plots of the Li//graphite cells before cycling indicate that the interfacial resistance is higher when using the pure PVDF membrane compared to the PVDF/graphene membrane (Fig. 8e and f). This suggests that the incorporation of graphene into the PVDF matrix facilitates the formation of a more uniform and stable electrode–electrolyte interface. In the case of the pure PVDF membrane, the semicircular impedance decreases with cycling, indicating the formation of an unstable SEI layer. In contrast, the PVDF/graphene membrane shows a slight decrease after the initial cycle and remains stable after 25 cycles, demonstrating that this membrane provides a stable interface during charge–discharge cycling, consistent with the SEM observations.

The thermal shrinkage of commercial PP and PVDF/graphene separators was evaluated under conventional heating at 27, 80, 120, and 140 °C, with each temperature held for 30 minutes. The optical images shown in Fig. S13 illustrate the behavior of both separators across this temperature range. The PP separator exhibited noticeable shrinkage at 140 °C, with the potential risk of damage at higher temperatures. In contrast, the PVDF/graphene separator displayed negligible shrinkage even at 140 °C, indicating its robustness under thermal stress.

Fig. S14 shows the charge–discharge profiles of the graphite electrode at different temperatures from 25 °C to 80 °C. An increase in charge-specific capacity is observed at 40 °C, indicating improved ionic conductivity at this temperature. However, above 60 °C, the charge-specific capacity decreases, along with irregular charge profiles, which suggests the occurrence of significant side reactions and electrolyte decomposition at higher temperatures.[60] Notably, the PVDF/graphene membrane remained intact and effectively prevented short-circuiting, demonstrating its thermal stability and potential for use in high-temperature environments. This enhanced thermal resistance suggests that the PVDF/graphene separator is a promising candidate for use in high-temperature batteries, as it effectively mitigates thermal shrinkage and reduces the risk of short circuits at elevated temperatures.

Several conclusions can be drawn by comparing the piezoelectric and electrochemical performance of the pure PVDF and PVDF/graphene membranes. Firstly, the PVDF/graphene nanocomposite membrane offers high piezoelectric potential and provides an efficient platform for PENGs. Secondly, the membrane exhibits enhanced electrolyte uptake and improved wettability with polar electrolytes, which boost ionic conductivity and promote stable SEI formation, thereby further enhancing electrochemical stability. Overall, the PVDF/graphene membrane offers high ionic conductivity, robust mechanical properties, excellent piezoelectric performance, and superior LIB performance.

Conclusions

A comparative study of pure PVDF and graphene nanosheet composite PVDF membranes is performed, where the incorporation of graphene nanosheets (0.05 wt%) into the PVDF matrix notably increased the β-phase content, thereby maximizing the piezoelectric voltage output compared to the pure PVDF membrane. Furthermore, the β-phase content increased further after electrical poling, leading to improved piezoelectric performance of the PVDF/graphene membrane. The PVDF/graphene composite membrane exhibited a more porous structure, enhanced surface wettability, and superior ionic conductivity, all contributed to improved lithium-ion transport properties, making it suitable for LIB applications. When employed in Li//Li cells, the composite membrane demonstrated enhanced cyclic stability with minimal potential variation. Additionally, in half and full cells, it delivered superior electrochemical performance, particularly in terms of cycling stability and rate capability. Overall, incorporating graphene into the PVDF matrix shows great potential for advancing next-generation PENGs, serving as a robust separator for LIBs, and enabling the development of self-charging power cells.

Conflicts of interest

There are no conflicts to declare.

Data availability

The data supporting this article have been included as part of the supplementary information (SI). Supplementary information is available. See DOI: **https://doi.org/10.1039/d5ma00960j**.

Acknowledgements

The authors acknowledge the financial support received from the National Centre for Photovoltaic Research and Education (NCPRE) and thank the Sophisticated Analytical Instrumentation Facility (SAIF) and Industrial Research & Consultancy Centre (IRCC) for material characterizations. The financial

support from the J. Gust. Richert Foundation (project number: 2023-00824) is gratefully acknowledged.

Open Access Article. Published on 03 December 2025. Downloaded on 2/12/2026 1:54:57 PM. This article is licensed under a Creative Commons Attribution-NonCommercial 3.0 Unported Licence.

References

1 D. Zhou, T. Yang, J. Yang and L. Z. Fan, *J. Mater. Chem. A*, 2020, **8**, 13267–13276.
2 X. Pu, L. Li, H. Song, C. Du, Z. Zhao, C. Jiang, G. Cao, W. Hu and Z. L. Wang, *Adv. Mater.*, 2015, **27**, 2472–2478.
3 T. T. Huang and W. Wu, *J. Mater. Chem. A*, 2019, **7**, 23280–23300.
4 H. He, Y. Fu, T. Zhao, X. Gao, L. Xing, Y. Zhang and X. Xue, *Nano Energy*, 2017, **39**, 590–600.
5 B. Mahanty, S. K. Ghosh, K. Maity, K. Roy, S. Sarkar and D. Mandal, *Mater. Adv.*, 2021, **2**, 4370–4379.
6 Z. Zhao, Y. Dai, S. X. Dou and J. Liang, *Mater. Today Energy*, 2021, **20**, 100690.
7 X. Wang, *Nano Energy*, 2012, **1**, 13–24.
8 H. Pei, J. Tan, Z. Peng, H. Zhang, S. Song, J. Guo, H. Lu, Z. Zheng, J. Jing, Y. Chen and Y. Xie, *Nano Energy*, 2025, **138**, 110847.
9 H. Zou, T. D. Nguyen and G. Pace, *MRS Bull.*, 2025, **50**, 295–304.
10 J. Chen, S. K. Oh, H. Zou, S. Shervin, W. Wang, S. Pouladi, Y. Zi, Z. L. Wang and J. H. Ryou, *ACS Appl. Mater. Interfaces*, 2018, **10**, 12839–12846.
11 L. Xing, Y. Nie, X. Xue and Y. Zhang, *Nano Energy*, 2014, **10**, 44–52.
12 X. Xue, S. Wang, W. Guo, Y. Zhang and Z. L. Wang, *Nano Lett.*, 2012, **12**, 5048–5054.
13 A. Rasheed, W. He, Y. Qian, H. Park and D. J. Kang, *ACS Appl. Mater. Interfaces*, 2020, **12**, 20891–20900.
14 D. Zhou, N. Wang, T. Yang, L. Wang, X. Cao and Z. L. Wang, *Mater. Horiz.*, 2020, **7**, 2158–2167.
15 N. Meng, X. Ren, G. Santagiuliana, L. Ventura, H. Zhang, J. Wu, H. Yan, M. J. Reece and E. Bilotti, *Nat. Commun.*, 2019, **10**, 4535.
16 N. A. Shepelin, P. C. Sherrell, E. N. Skountzos, E. Goudeli, J. Zhang, V. C. Lussini, B. Imtiaz, K. A. S. Usman, G. W. Dicinoski, J. G. Shapter, J. M. Razal and A. V. Ellis, *Nat. Commun.*, 2021, **12**, 3711.
17 Y. Fang, H. Zou, S. Peng, G. Dong and M. M. Tentzeris, *ACS Appl. Electron Mater.*, 2023, **5**, 4157–4167.
18 Y. Zhang, Y. Zhang, X. Xue, C. Cui, B. He, Y. Nie, P. Deng and Z. Lin Wang, *Nanotechnology*, 2014, **25**, 105401.
19 M. Kumar, N. D. Kulkarni and P. Kumari, *Mater. Today Proc.*, 2022, **56**, 1151–1155.
20 Q. Zhu, X. Song, X. Chen, D. Li, X. Tang, J. Chen and Q. Yuan, *Nano Energy*, 2024, **127**, 109741.
21 X. Song, B. Zhuo, S. Cao, L. Huang, Q. Zhu, J. Zhang and Q. Yuan, *Appl. Surf. Sci.*, 2024, **649**, 158996.
22 J. Yang, Y. Zhang, Y. Li, Z. Wang, W. Wang, Q. An and W. Tong, *Mater. Today Commun.*, 2021, **26**, 101629.
23 H. Y. Choi and Y. G. Jeong, *Composites, Part B*, 2019, **168**, 58–65.
24 H. Zhang, G. Tian, D. Xiong, T. Yang, S. Zhong, L. Jin, B. Lan, L. Deng, S. Wang, Y. Sun, W. Yang and W. Deng, *ACS Appl. Mater. Interfaces*, 2022, **14**, 29061–29069.
25 Y. Ahn, J. Y. Lim, S. M. Hong, J. Lee, J. Ha, H. J. Choi and Y. Seo, *J. Phys. Chem. C*, 2013, **117**, 11791–11799.
26 Q. Zhao, R. Zhou, C. Wang, J. Kang, Q. Zhang, J. Liu, Y. Jin, H. Wang, Z. Zheng and L. Guo, *Adv. Funct. Mater.*, 2022, **32**, 2112711.
27 W. Li, X. Li, X. Xie, A. Yuan and B. Xia, *Ionics*, 2017, **23**, 929–935.
28 J. Y. Kim, D. O. Shin, K. M. Kim, J. Oh, J. Kim, S. H. Kang, M. J. Lee and Y. G. Lee, *Sci. Rep.*, 2019, **9**, 1–7.
29 M. Yanilmaz, C. Chen and X. Zhang, *J. Polym. Sci., Part B: Polym. Phys.*, 2013, **51**, 1719–1726.
30 M. Palanisamy, V. P. Parikh, M. H. Parekh and V. G. Pol, *Energy Technol.*, 2020, **8**, 1–8.
31 Z. Liu, G. Li, Q. Qin, L. Mi, G. Li, G. Zheng, C. Liu, Q. Li and X. Liu, *Adv. Compos. Hybrid Mater.*, 2021, **4**, 1215–1225.
32 P. Wang, Y. Yin, L. Fang, J. He, Y. Wang, H. Cai, Q. Yang, Z. Shi and C. Xiong, *Composites, Part A*, 2014, **67**, 181–200.
33 J. Liu, X. Wu, J. He, J. Li and Y. Lai, *Electrochim. Acta*, 2017, **235**, 500–507.
34 M. Faraz, H. H. Singh and N. Khare, *J. Alloys Compd.*, 2021, **890**, 161840.
35 A. Kushwaha, M. K. Jangid, B. B. Bhatt, A. Mukhopadhyay and D. Gupta, *ACS Appl. Energy Mater.*, 2021, **4**, 7911–7921.
36 A. Kushwaha, A. Sharma, B. B. Bhatt, A. Mukhopadhyay and D. Gupta, *ACS Appl. Energy Mater.*, 2023, **6**, 4168–4178.
37 A. Valverde, R. Gonçalves, M. M. Silva, S. Wuttke, A. Fidalgo-Marijuan, C. M. Costa, J. L. Vilas-Vilela, J. M. Laza, M. I. Arriortua, S. Lanceros-Méndez and R. Fernández De Luis, *ACS Appl. Energy Mater.*, 2020, **3**, 11907–11919.
38 D. Li, D. Shi, Y. Xia, L. Qiao, X. Li and H. Zhang, *ACS Appl. Mater. Interfaces*, 2017, **9**, 8742–8750.
39 C. Fu, X. Zhang, H. Huo, J. Zhu, H. Xu, L. Wang, Y. Ma, Y. Gao, G. Yin, P. Zuo and J. Lu, *Adv. Funct. Mater.*, 2024, **34**, 2312187.
40 E. J. Yoo, J. Kim, E. Hosono, H. S. Zhou, T. Kudo and I. Honma, *Nano Lett.*, 2008, **8**, 2277–2282.
41 P. Guo, H. Song and X. Chen, *Electrochem. Commun.*, 2009, **11**, 1320–1324.
42 F. Torrisi, T. Hasan, W. Wu, Z. Sun, A. Lombardo, T. S. Kulmala, G. W. Hsieh, S. Jung, F. Bonaccorso, P. J. Paul, D. Chu and A. C. Ferrari, *ACS Nano*, 2012, **6**, 2992–3006.
43 E. B. Secor, P. L. Prabhumirashi, K. Puntambekar, M. L. Geier and M. C. Hersam, *J. Phys. Chem. Lett.*, 2013, **4**, 1347–1351.
44 Z. Liu, Y. Jiang, Q. Hu, S. Guo, L. Yu, Q. Li, Q. Liu and X. Hu, *Energy Environ. Mater.*, 2021, **4**, 336–362.
45 T. Sirichaibhinyo, S. Thiangtham, N. Saito and S. Ummartyotin, *Results Eng.*, 2024, **23**, 102807.
46 D. V. Horváth, R. Tian, C. Gabbett, V. Nicolosi and J. N. Coleman, *J. Electrochem. Soc.*, 2022, **169**, 030503.
47 A. Park, J. Y. Jung, S. Kim, W. J. Kim, M. Y. Seo, S. Kim, Y. J. Kim and W. B. Lee, *RSC Adv.*, 2023, **13**, 12917–12924.
48 R. Gregorio and M. Cestari, *J. Polym. Sci., Part B: Polym. Phys.*, 1994, **32**, 859–870.

© 2026 The Author(s). Published by the Royal Society of Chemistry

Open Access Article. Published on 03 December 2025. Downloaded on 2/12/2026 1:54:57 PM.
This article is licensed under a Creative Commons Attribution-NonCommercial 3.0 Unported Licence.

49 K. Shi, B. Chai, H. Zou, P. Shen, B. Sun, P. Jiang, Z. Shi and X. Huang, *Nano Energy*, 2021, **80**, 105515.
50 J. Yang, Y. Zhang, Y. Li, Z. Wang, W. Wang, Q. An and W. Tong, *Mater. Today Commun.*, 2021, **26**, 101629.
51 Q. Zhu, X. Song, X. Chen, D. Li, X. Tang, J. Chen and Q. Yuan, *Nano Energy*, 2022, **103**, 107807.
52 A. Gebrekrstos, T. S. Muzata and S. S. Ray, *J. Am. Chem. Soc.*, 2022, **5**, 7632–7651.
53 J. Q. Luo, H. F. Lu, Y. J. Nie, Y. H. Zhou, C. F. Wang, Z. X. Zhang, D. W. Fu and Y. Zhang, *Nat. Commun.*, 2024, **15**, 8636.
54 J. Zhang, X. Wang, X. Chen, X. Xia and G. J. Weng, *Energy Convers. Manage.*, 2022, **269**, 116121.
55 S. Song, Z. Zheng, Y. Bi, X. Lv and S. Sun, *J. Mater. Sci.*, 2019, **54**, 3832–3846.
56 C. Z. Zhao, X. Q. Zhang, X. B. Cheng, R. Zhang, R. Xu, P. Y. Chen, H. J. Peng, J. Q. Huang and Q. Zhang, *Proc. Natl. Acad. Sci. U. S. A.*, 2017, **114**, 11069–11074.
57 M. Agostini, S. Brutti and J. Hassoun, *ACS Appl. Mater. Interfaces*, 2016, **8**, 10850–10857.
58 W. H. Li, Q. L. Ning, X. T. Xi, B. H. Hou, J. Z. Guo, Y. Yang, B. Chen and X. L. Wu, *Adv. Mater.*, 2019, **31**, 1804766.
59 C. Yan, Y. X. Yao, W. L. Cai, L. Xu, S. Kaskel, H. S. Park and J. Q. Huang, *J. Energy Chem.*, 2020, **49**, 335–338.
60 Z. Xu, X. Zhang, J. Yang, X. Cui, Y. Nuli and J. Wang, *Nat. Commun.*, 2024, **15**, 9856.

© 2026 The Author(s). Published by the Royal Society of Chemistry